Current–Based Hybrid Moment Method Analysis of Electromagnetic Radiation and Scattering Problems

Ulrich Jakobus and Friedrich M. Landstorfer

Institut für Hochfrequenztechnik, Universität Stuttgart,
Pfaffenwaldring 47, 70550 Stuttgart, Germany

ABSTRACT. A current–based hybrid method combining the method of moments (MM) with asymptotic current expansions for the higher frequency range is presented for the analysis of arbitrarily shaped, three–dimensional, perfectly conducting electromagnetic radiation and scattering problems. Some examples demonstrate the drastic saving in memory requirement and CPU–time when applying the hybrid method as compared to the conventional MM. Even though the proposed method is a frequency domain formulation, some time domain results based on a Fourier transform are presented as they show an accurate description of diffracted and creeping waves.

1 Introduction

The MM [1] is a widely employed method to deal with perfectly conducting, lossy, or dielectric scattering problems either in the frequency or time domain. Here we will concentrate on three–dimensional, perfectly conducting bodies.

Rao et al. [2] proposed a current basis function $\vec{f}_n$ defined over triangular patches to deal with this type of problem in the frequency domain. The electric surface current density $\vec{J}$ is expressed as a linear superposition of basis functions

$$\vec{J} = \sum_{n=1}^{N} \alpha_n \cdot \vec{f}_n \qquad (1)$$

with unknown coefficients α_n. The electric field integral equation leads to a system of linear equations to determine these N unknown coefficients. Therefore, the memory requirement to store the elements of the matrix is of order N^2, and the CPU time to solve the system of linear equations is of order $N^{2...3}$, depending on the applied algorithm, e.g. Gauß elimination or conjugate gradient method.

The required number of triangular patches depends on the size of the scattering body with respect to the wavelength. In our experience, a value of about $N \approx 70 \ldots 100$ basis functions for modelling a surface with an area of a square wavelength λ^2 seems to be appropriate. This means that for a two–dimensional surface of fixed area the necessary number N of basis functions grows proportional to f^2, the square of the frequency. The result is a memory requirement proportional to f^4, and the CPU–time grows as $f^{4...6}$.

These dependencies obviously show that the conventional MM is restricted to the lower frequency range. The hybrid method proposed in the next section can overcome this difficulty.

2 Hybrid method

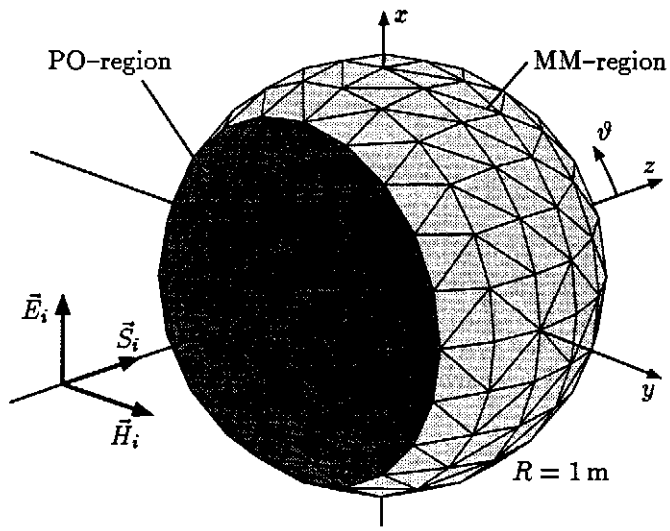

Fig. 1: Plane electromagnetic wave incident on a perfectly conducting sphere with radius $R = 1\,\mathrm{m}$.

Consider the example depicted in Fig. 1 where a plane electromagnetic wave is incident on a perfectly conducting sphere with radius $R = 1\,\mathrm{m}$. The surface of the sphere has been subdivided into triangular patches, where basis functions $\vec{f}_n$ according to Ref. [2] are applied in eqn. (1) to represent the current density $\vec{J}$ on the surface of the sphere.

Ray–based hybrid methods combining the MM with the geometrical theory of diffraction [3, 4, 5] are not very

suitable to deal with this class of problems involving one large scattering body. Their scope of application is, for instance, radiation problems with an antenna located in front of a large scatterer. Here, however, current–based hybrid methods [6, 7, 8, 9, 10] seem to be more advantageous. As depicted in Fig. 1, we can subdivide the surface into a MM– (light shading) and a PO–region (dark shading), where the physical optics approximation is applied.

In general, the MM–region may consist of wires and surfaces while the PO approximation can be applied only to surfaces. We subdivide metallic wires into electrically short segments and employ triangular basis functions to represent the electric current I^{MM}. On the surfaces in both regions we use an expansion according to eqn. (1) for the surface current density:

$$\vec{J}^{MM} = \sum_{n=1}^{N^{MM}} \alpha_n \cdot \vec{f}_n \tag{2}$$

$$\vec{J}^{PO} = \sum_{n=N^{MM}+1}^{N^{MM}+N^{PO}} \alpha_n \cdot \vec{f}_n. \tag{3}$$

Every basis function $\vec{f}_n$ extends over two adjacent triangular patches [2]. Basis functions located at the boundary between the MM– and the PO–region, i.e. one of the two patches lies in the PO–region and the other in the MM–region, are assigned to the MM–region. This allows a continuous current modeling across the boundary.

Only the N^{MM} unknown coefficients α_n in eqn. (2) are determined by solving a system of linear equations which results from the electric field integral equation and a Galerkin testing procedure. The remaining N^{PO} coefficients α_n in eqn. (3) are based on the physical optics approximation

$$\vec{J}^{PO}(\vec{r}) = 2\,\delta_i \cdot \hat{n} \times \vec{H}_i(\vec{r}) + \sum_{n=1}^{N^{MM}} 2\,\alpha_n\,\delta_n \cdot \hat{n} \times \vec{\mathcal{H}}\left\{\vec{f}_n\right\}. \tag{4}$$

The first contribution in eqn. (4) represents the conventional PO current density caused by the incident magnetic field strength $\vec{H}_i$ of the excitation. The vector $\hat{n}$ denotes a unit vector normal to the surface at the observation point $\vec{r}$. A coefficient δ_i accounts for shadowing effects. If $\vec{r}$ lies in the shadowed region, δ_i must be set to zero. Otherwise δ_i equals ± 1, the sign depending on the direction of incidence with respect to the orientation of $\hat{n}$.

The second contribution in eqn. (4) accounts for the coupling between the MM– and the PO–region. A summation takes place over basis functions $\vec{f}_n$ in the MM–region with respective coefficients α_n. The operator $\vec{\mathcal{H}}$ acting on $\vec{f}_n$ yields the magnetic field strength caused by the basis function $\vec{f}_n$ and can be expressed as

$$\vec{\mathcal{H}}\left\{\vec{f}_n\right\} = -\frac{1}{4\pi} \iint_{A'} \vec{f}_n(\vec{r}\,') \times \vec{\nabla} G(\vec{r}, \vec{r}\,')\, dA' \tag{5}$$

with the free space Green's function

$$G(\vec{r}, \vec{r}\,') = \frac{e^{-j\beta|\vec{r}-\vec{r}\,'|}}{|\vec{r}-\vec{r}\,'|} \tag{6}$$

and the wave number $\beta = \frac{2\pi}{\lambda}$. The vector product $2\hat{n}\times$ in eqn. (4) leads to the PO–current density. Again, coefficients δ_n must be considered to account for shadowing effects.

The coefficients α_n in eqn. (3) can be obtained directly from eqn. (4), thus circumventing the process of solving a system of linear equations.

All further details of the hybrid method can be found in Ref. [11]. In that paper we also developed correction terms $\vec{J}^{FW}$ (fringe wave) based on the exact solution for the half–plane scattering problem to account for effects of edges of polygonal plates. Further correction terms to consider the edges of perfectly conducting wedges are presented in Ref. [12]. The following examples show that these high frequency current approximations implemented in a hybrid method together with the MM represent a powerful tool for the analysis of a wide variety of electromagnetic radiation and scattering problems.

3 Examples

The first example has already been depicted in Fig. 1. The perfectly conducting sphere of radius $R = 1\,\mathrm{m}$ is subdivided into 368 triangular patches resulting in 552 basis functions $\vec{f}_n$ associated with the interior edges between the triangular patches. A plane electromagnetic wave polarized in x–direction and propagating in positive z–direction is incident on the sphere.

We have chosen this particular example because the results can be compared to the exact solution available in the literature (e.g. Ref. [13]). First we have calculated the monostatic radar cross section (RCS) σ of the sphere in the frequency domain using the MM or the PO approximation, respectively, on the entire surface of the sphere, i.e. contrary to Fig. 1 no subdivision into a MM– and a PO–region has been made.

The result is depicted in Fig. 2. It shows an excellent agreement between the exact solution (dash–dotted line)

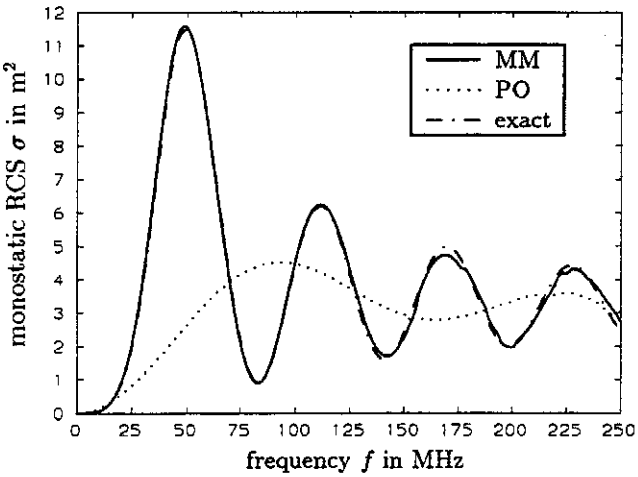

Fig. 2: Monostatic radar cross section σ of the sphere as a function of the frequency f.

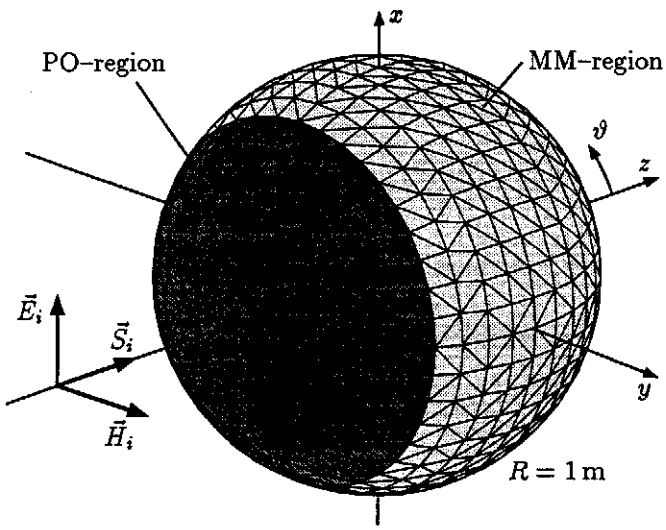

Fig. 3: Adaptive subdivision of the surface of the sphere into triangular patches (1272 triangles here, 368 patches in Fig. 1).

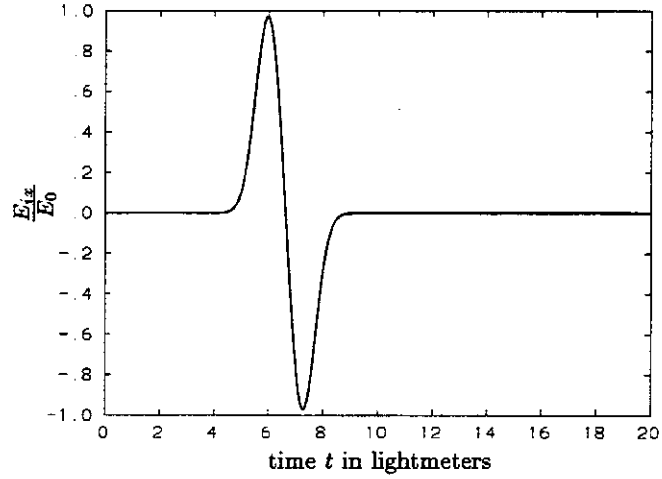

Fig. 4: Pulse incident on the sphere according to eqn. (7) at the origin $\vec{r} = 0$ with $a = 1.5\,\frac{1}{\mathrm{m}}$, $t_1 = 6\,\mathrm{lm}$, and $t_2 = 7.25\,\mathrm{lm}$.

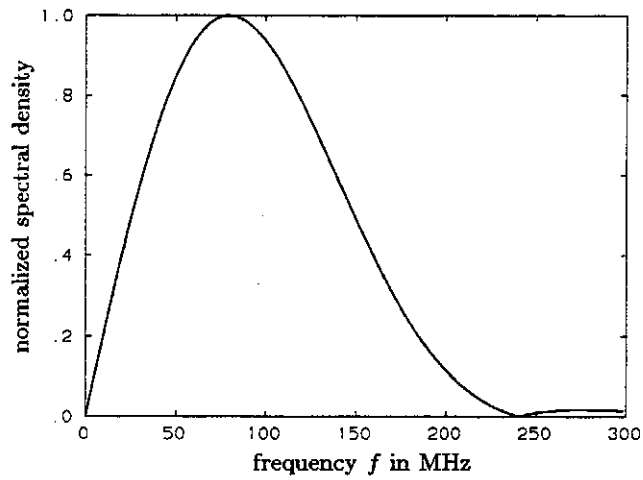

Fig. 5: Normalized spectral density for the pulse according to eqn. (7) with $a = 1.5\,\frac{1}{\mathrm{m}}$, $t_1 = 6\,\mathrm{lm}$, and $t_2 = 7.25\,\mathrm{lm}$ as depicted in Fig. 4.

and the MM solution (solid line). The PO solution (dotted line) fails, mainly because of the small size of the sphere. At $f = 150\,\mathrm{MHz}$ the diameter of the sphere just equals one wavelength λ.

It should be noted that the implemented computer code allows an adaptive segmentation based on the actual value of the wavelength. When dealing with low frequencies the sphere is subdivided into 368 patches as shown in Fig. 1. With increasing frequency the program automatically chooses a larger number of patches, e.g. at 500 MHz 1272 triangles are used as depicted in Fig. 3. This varying number of patches causes the small jumps that can be observed in the MM–solution in Fig. 2 e.g. at about 225 MHz.

Now we will investigate the time domain response when a pulse described by

$$\vec{E}_i(\vec{r},t) = \vec{E}_0 \cdot \left(e^{-a^2[c\,(t-t_1)-\vec{r}\cdot\hat{\beta}]^2} - e^{-a^2[c\,(t-t_2)-\vec{r}\cdot\hat{\beta}]^2} \right) \tag{7}$$

with $a = 1.5\,\frac{1}{\mathrm{m}}$, $t_1 = 20\,\mathrm{ns}$, $t_2 = 24.18\,\mathrm{ns}$, $\vec{E}_0 = E_0\,\hat{x}$, and $\hat{\beta} = \hat{z}$ is incident on the sphere. c denotes the velocity of light in free space. It is useful to specify the time t in units of lightmeters (lm) with $1\,\mathrm{lm} = \frac{1\,\mathrm{m}}{c} \approx 3.34\,\mathrm{ns}$. Thus we have $t_1 = 6\,\mathrm{lm}$ and $t_2 = 7.25\,\mathrm{lm}$.

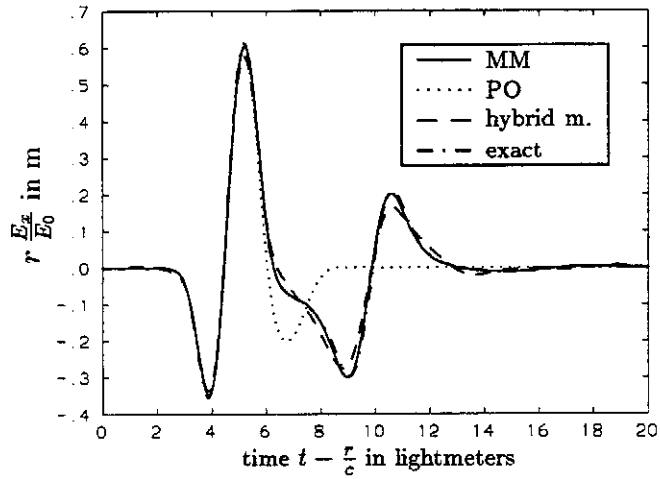

Fig. 6: Backscattered pulse in the farfield as a function of time for the pulse according to Fig. 4 incident on the perfectly conducting sphere.

Fig. 4 shows the shape of the incident pulse as a function of time. The corresponding normalized spectral density is depicted in Fig. 5. We have chosen two successive Gauß pulses with a time delay of $t_2 - t_1 = 1.25\,\mathrm{lm}$ so that the spectral intensity is maximum at about 79 MHz.

The backscattered pulse in the farfield region can be calculated by means of Fourier transforming the complex frequency response, as depicted in Fig. 2, multiplied with the complex spectral intensity of the excitation. The result is shown in Fig. 6, where r denotes the distance of the observation point in the farfield. The time t is shifted by $\frac{r}{c}$ so that $t-\frac{r}{c}=0$ describes the propagation of a pulse starting at $t=0$ at the origin of the coordinate system or at the center of the sphere, respectively. Looking at Fig. 3, we can see that the maximum of the incident wave at $t = 6\,\mathrm{lm}$ in Fig. 4 is reflected at the point $x = y = 0$ and $z = -R = -1\,\mathrm{m}$ at the time $t = 5\,\mathrm{lm}$. This reflected wave can be observed in the farfield at the time $t - \frac{r}{c} = 4\,\mathrm{lm}$, which is in accordance with the calculated response in Fig. 6.

The solid line in Fig. 6 represents a solution based on an application of the MM on the whole surface of the sphere, i.e. no asymptotic current expansion is involved. This curve is in excellent agreement with the exact result (dash-dotted line). The dotted line is the result of the PO approximation on the whole surface of the sphere. This solution differs distinctly from the exact result for times $t - \frac{r}{c} > 6\,\mathrm{lm}$. The additional negative peak of the exact solution at $t - \frac{r}{c} \approx 9\,\mathrm{lm}$ can be interpreted as a creeping wave with a time delay of $\frac{\pi R}{c} \approx 3.14\,\mathrm{lm}$ arriving at $t - \frac{r}{c} \approx (6 + 3.14)\,\mathrm{lm}$ in the farfield region. This creeping wave term is absent in the PO solution.

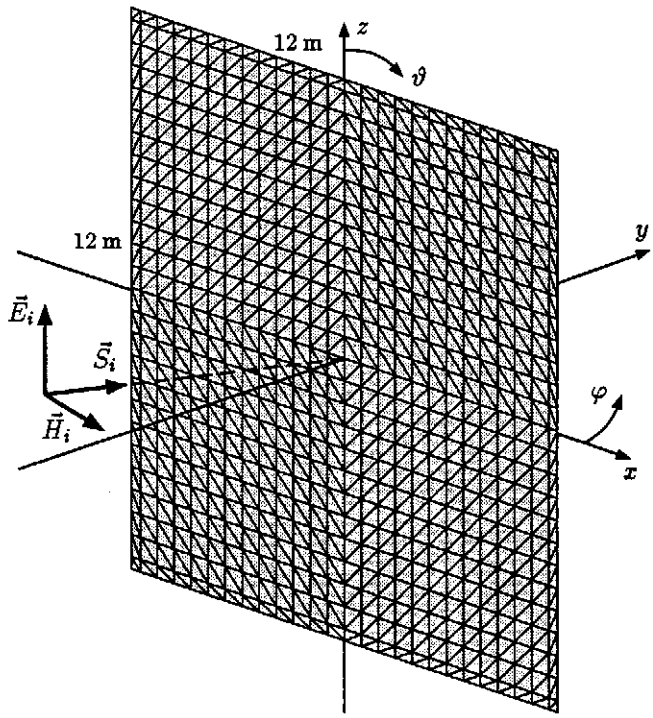

Fig. 7: Plane electromagnetic wave incident on a perfectly conducting square plate with side length 12 m.

Now we will demonstrate the application of the hybrid method. For frequencies lower than 75 MHz (compare to Fig. 5) we employ the conventional MM for the whole surface of the sphere. This is not a disadvantage, as we make use of an adaptive segmentation scheme and for these low frequencies only a moderate number of unknowns is required. The hybrid method is used for frequencies above 75 MHz. The range $0° \leq \vartheta \leq 120°$ in Fig. 3 represents the MM–region while PO is applied on the remaining part of the surface (dark shading). The resulting backscattered pulse is depicted in Fig. 6 by the dashed line. Good agreement with the exact solution can be observed also for times $t - \frac{r}{c} > 6\,\mathrm{lm}$ when PO fails.

A second example is shown in Fig. 7. A plane electromagnetic wave according to eqn. (7) with $a = 1\,\frac{1}{\mathrm{m}}$, $t_1 = 6\,\mathrm{lm}$, and $t_2 = 8\,\mathrm{lm}$ is incident on a perfectly conducting square plate with side length 12 m. First the case of perpendicular incidence with $\vartheta_i = 90°$ and $\varphi_i = 270°$ will be considered, i.e. the wave is propagating in positive y–direction with $\vec{E}_0 = E_0\,\hat{z}$ and $\hat{\beta} = \hat{y}$ in eqn. (7).

The backscattered pulse in the farfield region is depicted in Fig. 8. The solid line corresponds to the solution based on the MM applied to the entire structure. The dotted curve is the result of the PO approximation $J_z^{PO} = 2\,H_{ix}$. We can modify this PO current density by a heuristic superposition of correction terms $\vec{J}^{FW}$ asso-

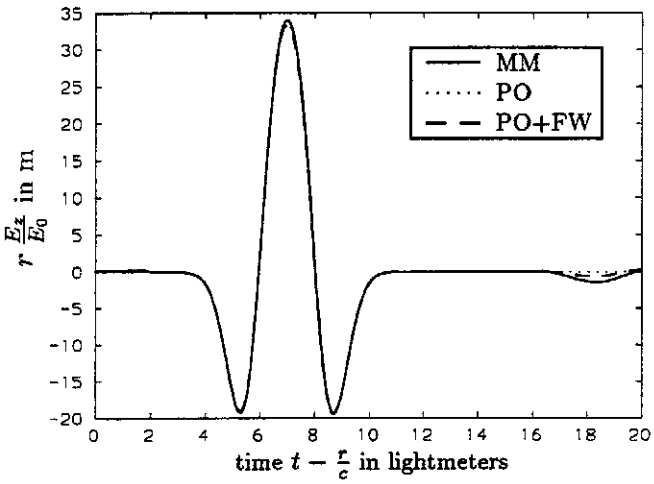

Fig. 8: Backscattered pulse in the farfield as a function of time for the perfectly conducting plate with perpendicular incidence.

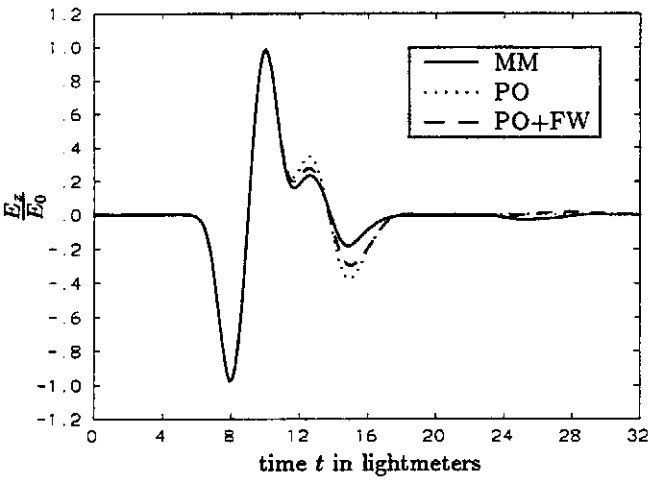

Fig. 9: Scattered pulse in the nearfield at an observation point $x = z = 0$ and $y = -2\,\mathrm{m}$ as a function of time for the perfectly conducting plate with perpendicular incidence.

ciated with the four edges of the plate [11]. This leads to the dashed line in Fig. 8. If we try to interpret the results with diffraction theory, we find one reflected and four edge diffracted rays that overlap because of the same time delay for an observation point on the negative y–axis in the far field. The double diffracted rays have an additional time delay of 12 lm and can be observed in Fig. 8 at $t - \frac{r}{c} \approx 18\,\mathrm{lm}$.

We can separate the reflected pulse and the four edge diffracted pulses by choosing an observation point in the nearfield. Fig. 9 shows the scattered field at an observation point $x = z = 0$ and $y = -2\,\mathrm{m}$. The maximum of

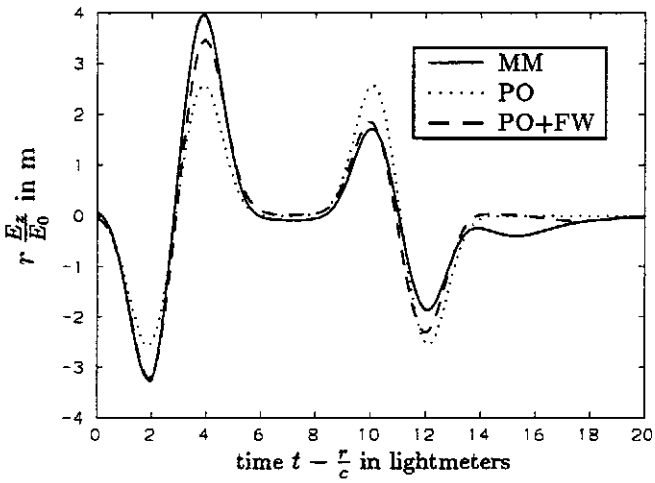

Fig. 10: Backscattered pulse in the farfield as a function of time for the perfectly conducting plate with direction of incidence $\vartheta_i = 90°$ and $\varphi_i = 250°$.

the incident pulse, which is reflected at $t = t_1 = 6\,\mathrm{lm}$, arrives at the observation point at $t = 8\,\mathrm{lm}$. The first maximum of the four edge diffracted pulses can be observed at $t = (6 + \sqrt{6^2 + 2^2})\,\mathrm{lm} \approx 12.32\,\mathrm{lm}$, whereas the double diffracted pulses arrive at $t \approx 24.32\,\mathrm{lm}$.

The two figures 8 and 9 show that the agreement between the MM solution acting as reference and the PO solution is very accurate concerning the reflected pulse. However, this is not true for other than perpendicular incidence.

Fig. 10 shows the monostatic backscattered pulse in the farfield for the direction of incidence $\vartheta_i = 90°$ and $\varphi_i = 250°$. If we try to interpret this figure with diffraction theory, we find that for the first maximum of the incident pulse at $t = 6\,\mathrm{lm}$ a diffraction process at the point $x = -6\,\mathrm{m}$ and $y = z = 0$ takes place. The farfield response can be observed at $t - \frac{r}{c} = (6 - 2 \cdot 6 \sin 20°)\,\mathrm{lm} \approx 1.9\,\mathrm{lm}$. This time agrees well with Fig. 10, but we can observe that the amplitude of the pulse based on the PO solution (dotted line) differs from the MM solution (solid line). Only through the superposition of correction terms (dashed line) can the amplitude be improved. This applies equally to the second pulse caused by a diffraction process at the point $x = 6\,\mathrm{m}$ and $y = z = 0$, which can be observed in Fig. 10 at $t - \frac{r}{c} = (6 + 2 \cdot 6 \sin 20°)\,\mathrm{lm} \approx 10.1\,\mathrm{lm}$.

A further example is shown in Fig. 11. A backfire Yagi–Uda antenna consisting of three shape optimized elements [14, 15] is located in front of a perfectly conducting square plate with a side length of 3λ. As opposed to the previous examples, we will restrict our investigations to one single frequency.

The radiation patterns in the E– and H–plane of the

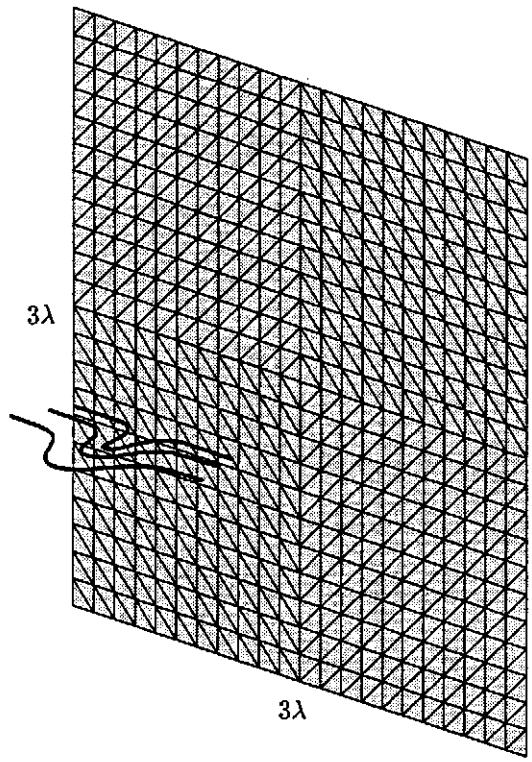

Fig. 11: Backfire Yagi–Uda antenna of three shaped optimized elements in front of a reflector of size $3\lambda \times 3\lambda$.

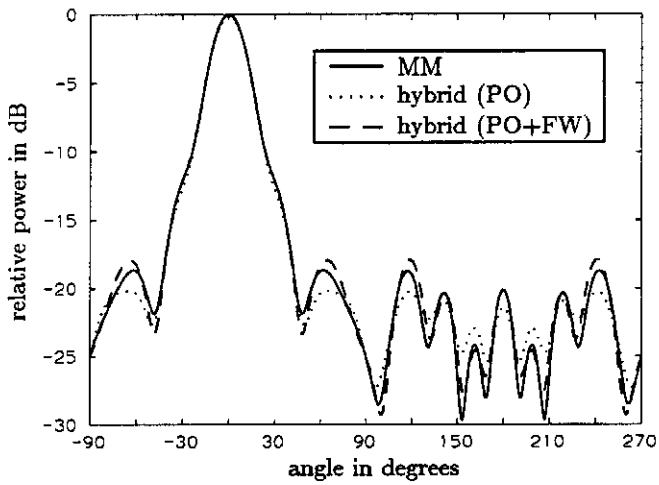

Fig. 12: E-plane radiation pattern of the shape optimized Yagi–Uda antenna in front of a reflector.

Yagi–Uda antenna are depicted in Fig. 12 and 13, respectively. The solid line results from a calculation based on the conventional MM. Applying the hybrid method proposed in Section 2, we assign the wire antenna to the MM–region and the surface of the reflector to the PO–region. This yields a radiation pattern shown by

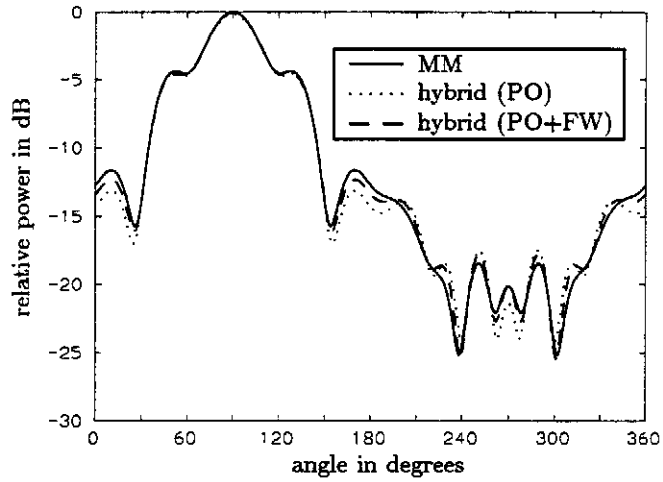

Fig. 13: H-plane radiation pattern of the shape optimized Yagi–Uda antenna in front of a reflector.

Table 1: Input impedance, gain, memory requirement and CPU–time for the backfire Yagi–Uda array in front of a reflector.

	MM	hybrid method PO	hybrid method PO+FW
input impedance in Ω			
real part	15.6	15.4	15.5
imaginary part	-56.9	-56.8	-56.9
gain in dB	12.67	12.47	12.62
no. of basis functions			
MM–region	1494	86	86
PO–region	–	1408	1408
number of unknowns (exploiting symmetry)	397	45	45
memory for matrix in kByte	2463	32	32
CPU-time in sec (HP 9000/710)	380	163	325

the dotted lines in Figs. 12 and 13. Superimposing additional correction terms $\vec{J}^{FW}$ to the PO current density on the surface of the plate leads to the results depicted by dashed lines.

Values of the input impedance and the gain of the antenna as obtained by the three methods are tabulated in Table 1.

In the introduction we claimed that the application of the hybrid method leads to a drastic reduction in memory requirement and CPU time as compared to the conventional MM. This is confirmed in Table 1. 86 triangular

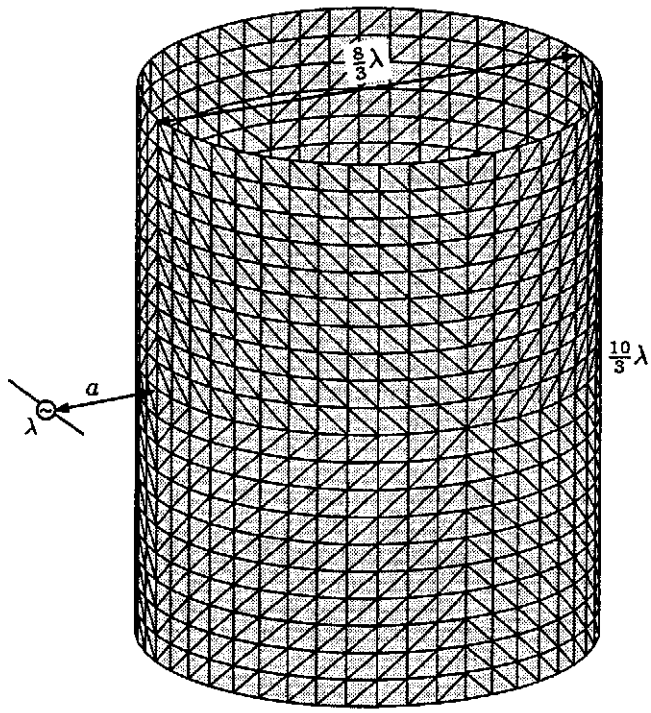

Fig. 14: λ–dipole antenna in front of a circular cylinder of finite length with variable distance a.

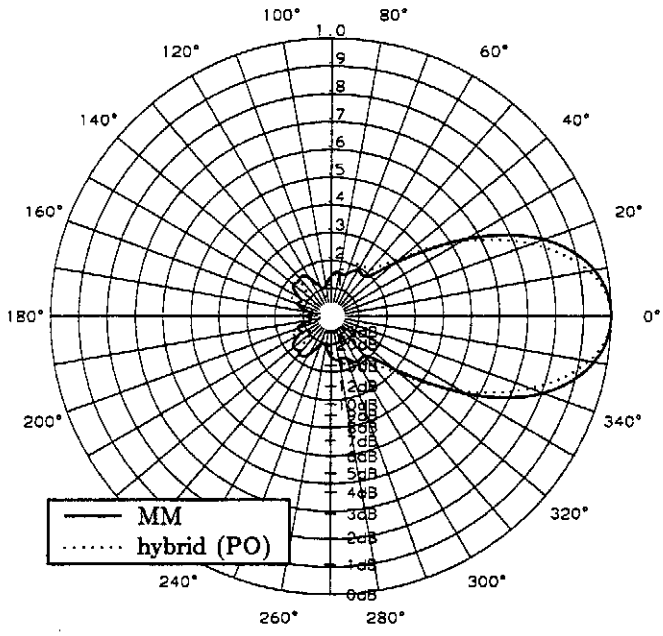

Fig. 15: E–plane radiation pattern of the λ–dipole antenna in front of a circular cylinder ($a = 0.7\,\lambda$).

basis functions defined along the wire segments are required to model the wire antenna. On the surface of

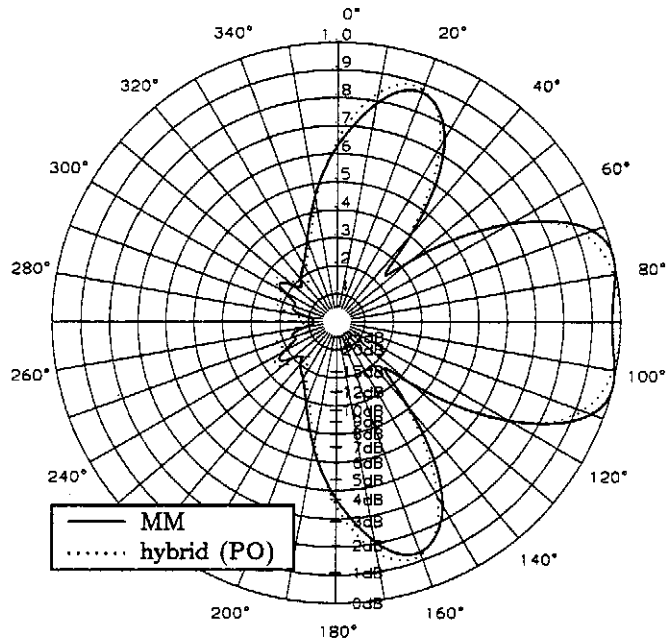

Fig. 16: H–plane radiation pattern of the λ–dipole antenna in front of a circular cylinder ($a = 0.7\,\lambda$).

the reflector 1408 basis functions $\vec{f}_n$ are used leading to a total number of 1494 basis functions for the conventional MM. Exploiting symmetry of the structure, the total number of unknown coefficients which have to be calculated from the solution of a system of linear equations can be reduced to 397. When applying the hybrid method, this number equals 45. Consequently, we have a reduction in memory requirement for the matrix of the system of linear equations by a factor of about 77.

Finally, one last example shown in Fig. 14 shall be investigated. A λ–dipole antenna is located in front of a circular cylinder of finite length with variable distance a. The cylinder has a diameter of $\frac{8}{3}\lambda$ and a height of $\frac{10}{3}\lambda$.

When applying the hybrid method, the dipole antenna represents the MM–region and the PO–region consists of the surface of the cylinder. Note that we have used conventional PO on the cylindrical surface. Similar to accounting for effects of edges of polygonal plates by correction terms $\vec{J}^{FW}$, we are presently investigating the improvement of the PO–current for curved surfaces by correction terms derived from the Fock theory [16]. Results will be reported in an upcoming paper.

The four figures 15–18 show the E–plane and H–plane radiation pattern, respectively, for the two distances $a = 0.7\,\lambda$ and $a = 0.9\,\lambda$, respectively. The solid line is based on a calculation with the conventional MM whereas the dotted curve shows the result of the hybrid method. Good agreement can be observed.

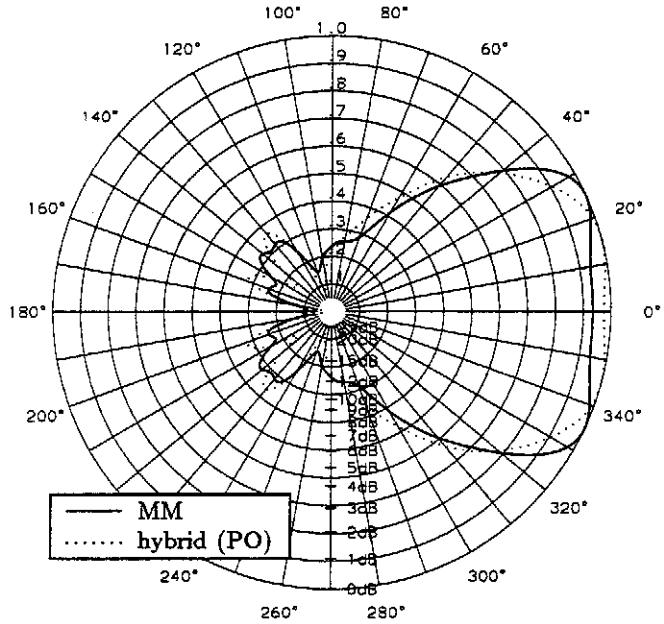

Fig. 17: E–plane radiation pattern of the λ–dipole antenna in front of a circular cylinder ($a = 0.9\,\lambda$).

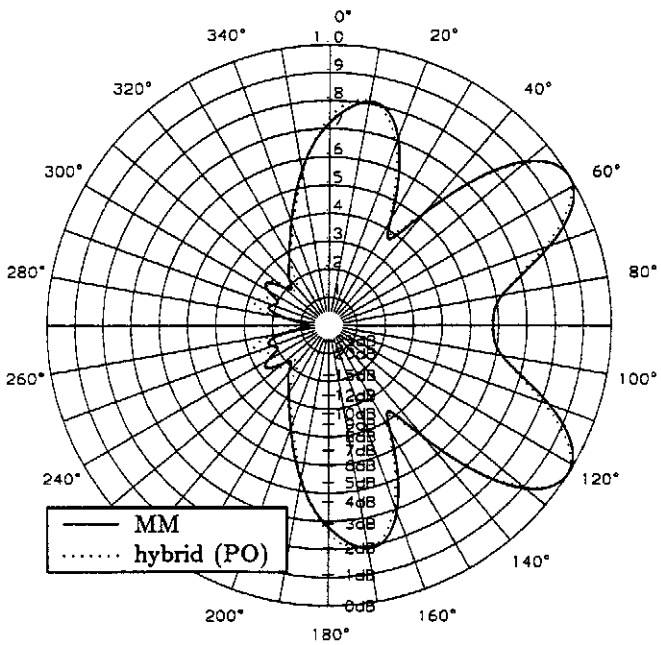

Fig. 18: H–plane radiation pattern of the λ–dipole antenna in front of a circular cylinder ($a = 0.9\,\lambda$).

Table 2 summarizes memory requirement and CPU–time for this example.

Table 2: Memory requirement and CPU–time for the λ–dipole antenna in front of a circular cylinder.

	MM	hybrid m.
number of basis functions		
MM–region	2852	20
PO–region	–	2832
number of unknowns (exploiting symmetry)	726	11
memory for matrix in kByte	8236	2
CPU-time in sec (HP 9000/735)	258	54

4 Conclusions

A hybrid method has been presented combining the MM with asymptotic current expansions for the higher frequency range. In the simplest case the conventional PO approximation is employed. For polygonal scattering bodies we have improved the asymptotic PO current density by heuristic correction terms to take the effects of edges into account. Currently we are also investigating the application of Fock currents for curved surfaces.

Some examples have demonstrated the accuracy of the hybrid method as compared to the conventional MM even though a drastic reduction in memory requirement and CPU-time can be achieved. Some computational results have been transformed from the frequency domain into the time domain allowing a physical interpretation with diffraction theory considering reflected, creeping and diffracted waves.

References

[1] R. F. Harrington, *Field Computation by Moment Methods*. Macmillan Company, New York, 1968.

[2] S. M. Rao, D. R. Wilton, and A. W. Glisson, "Electromagnetic scattering by surfaces of arbitrary shape," *IEEE Transactions on Antennas and Propagation*, vol. 30, pp. 409–418, May 1982.

[3] W. D. Burnside, C. L. Yu, and R. J. Marhefka, "A technique to combine the geometrical theory of diffraction and the moment method," *IEEE Transactions on Antennas and Propagation*, vol. 23, pp. 551–558, July 1975.

[4] G. A. Thiele and T. H. Newhouse, "A hybrid technique for combining moment methods with the geometrical theory of diffraction," *IEEE Transactions on Antennas and Propagation*, vol. 23, pp. 62–69, Jan. 1975.

[5] J. N. Sahalos and G. A. Thiele, "On the application of the GTD–MM technique and its limitations," *IEEE Transactions on Antennas and Propagation*, vol. 29, pp. 780–786, Sept. 1981.

[6] L. N. Medgyesi-Mitschang and D.-S. Y. Wang, "Review of hybrid methods on antenna theory," *Annales des Télécommunications*, vol. 44, no. 9-10, pp. 445–455, 1989.

[7] L. N. Medgyesi-Mitschang and D.-S. Wang, "Hybrid methods in computational electromagnetics: a review," *Computer Physics Communications*, vol. 68, pp. 76–94, 1991.

[8] C. S. Kim and Y. Rahmat-Samii, "Low profile antenna study using the physical optics hybrid method (POHM)," in *IEEE International Symposium on Antennas and Propagation, London, Ontario*, pp. 1350–1353, June 1991.

[9] U. Jakobus, J. Christ, and F. M. Landstorfer, "PO–MoM analysis of cavity–backed antennas," in *ICAP '93, IEE 8th International Conference on Antennas and Propagation, Edinburgh, Conf. Publication Number 370*, pp. 111–114, Apr. 1993.

[10] L. N. Medgyesi-Mitschang and J. M. Putnam, "Hybrid formulation for arbitrary 3–D bodies," in *10th Annual Review of Progress in Applied Computational Electromagnetics, ACES Conference, Monterey*, vol. II, pp. 267–274, Mar. 1994.

[11] U. Jakobus and F. M. Landstorfer, "Improved PO–MM hybrid formulation for scattering from three–dimensional perfectly conducting bodies of arbitrary shape," *IEEE Transactions on Antennas and Propagation*, vol. 43, pp. 162–169, Feb. 1995.

[12] U. Jakobus and F. M. Landstorfer, "Correction of the PO current density close to perfectly conducting wedges by the UTD," *Electronics Letters*, vol. 30, pp. 2111–2112, Dec. 1994.

[13] R. F. Harrington, *Time Harmonic Electromagnetic Fields*. McGraw Hill, New York, 1961.

[14] F. M. Landstorfer, "A new type of directional antenna," in *IEEE Symposium on Antennas and Propagation, Mass., USA*, pp. 169–172, Oct. 1976.

[15] F. M. Landstorfer and R. R. Sacher, *Optimisation of Wire Antennas*. Research Studies Press, John Wiley & Sons, New York, 1985.

[16] V. A. Fock, *Electromagnetic Diffraction and Propagation Problems, International Series of Monographs on Electromagnetic Waves*, vol. 1. Pergamon Press, Oxford, 1965.